Charge carrier recombination at perovskite/HTL interfaces monitored by time-resolved spectroscopy

Jafar I. Khan*, Furkan H. Isikgor, Esma Ugur, Waseem Raja, George T. Harrison, Emre Yengel, Thomas D. Anthopoulos, Stefaan De Wolf, Frédéric Laquai*

King Abdullah University of Science and Technology (KAUST), KAUST Solar Center (KSC), Physical Sciences and Engineering Division (PSE), Thuwal 23955-6900, Kingdom of Saudi Arabia

Corresponding authors:
frederic.laquai@kaust.edu.sa
jafar.khan@kaust.edu.sa

Abstract

Carrier recombination at the interface between charge extraction layers and the perovskite photoactive layer in solar cells reduces the quasi-Fermi level splitting (QFSL) and hence, the device's open-circuit voltage (V_{OC}). Distinguishing between interfacical carrier recombination and charge extraction requires selective probing of carrier dynamics with transient optical spectroscopy techniques. However, bulk recombination, interfacial recombination, and charge extraction all contribute to the transient response making a precise determination of individual rates challenging. Here, we compare two commonly-used hole transport layers (HTLs), namely, PTAA and NiO_x, adjacent to prototypic $MAPI_3$ perovskite photoactive layers and wide-bandgap perovskites. We demonstrate that combining time-resolved photoluminescence (TR-PL) and transient absorption (TA) measurements can reveal recombination losses associated with the perovskite/NiO_x interface, as confirmed by drift-diffusion simulations. The best performing $MAPI_3$/PTAA-based device exhibits less non-radiative recombination and more efficient charge extraction, facilitated by favorable energy level alignment.

TOC

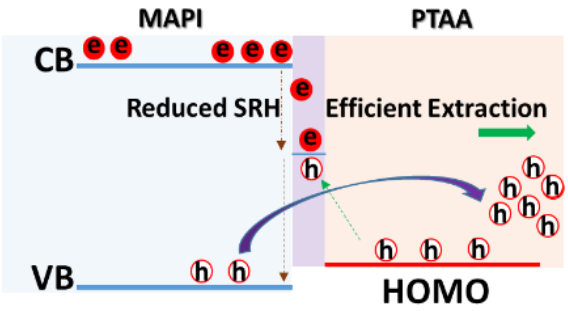

Perovskite solar cells (PSCs) have attracted immense attention in the last decade due to their outstanding optical and electronic properties, and the rapidly increasing power conversion efficiency (PCE), today in the range of 25.5% for single-junction devices.[1] PSCs are fabricated either in *n-i-p* or *p-i-n* configuration, referring to the position of the charge transport layers (CTLs). Although the highest PCEs have been reported for the *n-i-p* structure, the *p-i-n* configuration is said to be industrially more relevant. It offers several advantages such as the possibility of low-temperature processing, dopant-free manufacturing, and compatibility with already existing organic electronic manufacturing processes.[2] Currently, the most widely and efficient HTL employed in *p-i-n* based PSCs is a compact layer of poly[bis(4-phenyl)-(2,4,6-trimethylphenyl)amine] (PTAA).[3, 4] This polymer has proven to be more efficient as compared to the conventional poly(3,4-ethylenedioxythiophene)polystyrene sulfonate (PEDOT:PSS) or nickel oxide (NiO_x). On the other hand, the high optical transparency, superior solvent tolerance, and stability of NiO_x, make it appealing for efficient and stable *p-i-n* tandem devices.[5] Fundamental studies have addressed the importance of selective HTLs, specifically on the interfacial physical processes.[6,7] The interface between the CTL and the absorber (perovskite) layer induces additional non-radiative recombination pathways such as trap-assisted recombination, which limits the open-circuit voltage (V_{OC}) of devices.[8] Furthermore, other effects such as interface-charging have been reported in literature.[9] These trap states are also responsible for the lower stability of the respective PSCs.[10]

Numerous studies have reported state-of-the-art HTLs including small organic molecules, polymers, and metal oxides, however, several induce non-radiative losses, which can be detrimental for the device's PCE.[6,11] Hence, reducing interface recombination is of utmost importance in the design of HTLs.[12] Additionally, band alignment is a critical parameter for charge selectivity, and a favorable alignment of the energy level of the HTL with the perovskite absorber layer ensures efficient charge extraction.[13,14] In case of organic HTLs, the ground state bleach (GSB) observed by transient absorption (TA) spectroscopy can be used to probe the hole transfer process and recombination dynamics.[15] However, inorganic metal oxides do not display a GSB, their excited state absorption cross-sections are small, and the excited state spectra overlap with their ground state absorption in the spectral range of 300–400 nm. Hence, spectroscopically differentiating charge extraction from interface recombination losses becomes a challenge when using inorganic HTLs.

Identifying the precise loss mechanisms is a prerequisite to further advance PCEs in PSCs. Interfacial recombination and charge extraction are competing processes, which are not easily distinguishable in transient optical spectroscopy. However, combining data from different time-resolved techniques such as photoluminescence (TR-PL) and TA spectroscopy can help to disentangle the loss processes.[16,17] In TRPL and TA, both extraction and recombination reduce the lifetime of the PL, thus causing a faster signal decay.[18] Moreover, V_{OC} and quasi-Fermi level splitting (QFLS) in the absorber layer are typically in the same order in highly efficient devices, while poor devices exhibit lower QFLS.[6,19]

Herein, we report the impact of two different HTLs, precisely, NiO_x and PTAA, adjacent to two different perovskite (PVK) materials, namely, $MAPbI_3$ (MAPI) and the wide bandgap (WBG) multi-cation lead mixed halide perovskite $Cs_{0.15}MA_{0.15}FA_{0.70}Pb(I_{0.80}Br_{0.20})_3$; the latter finds application in multi-junction tandem solar cells.[20] By combining TR-PL and TA spectroscopy results, the origin of higher J_{SC} (23.6 mA/cm^2) and V_{OC} (1.13 V) in MAPI/PTAA based devices is unraveled. In particular, we demonstrate that interfacial charge recombination and extraction can be distinguished by this approach. Specifically, when exciting the samples from the HTL side, extraction is effectual, while non-radiative recombination is significantly reduced in MAPI/PTAA-based devices compared to both WBG/NiO_x and MAPI/NiO_x solar cells. Finally, our drift-diffusion device simulation exposed a more favorable energy level alignment at the MAPI/PTAA interface. In contrast, from the drift-diffusion simulation, significant energy offsets (ΔE) were found between the PVK and NiO_x valence bands, more precisely, 50 meV and 70 meV for MAPI and WBG, respectively. This rationalizes the losses in V_{OC} and supports the observation of interfacial non-radiative recombination by time-resolved measurements caused by charge accumulation in combination with a high surface recombination velocity. Impedance spectroscopy measurements further support this claim, indicating a higher resistance at the MAPI/PTAA interface in turn resulting in lower trap density compared to MAPI/NiO_x.

We studied the steady-state optical characteristics of representative MAPI and WBG perovskite absorber layers. The UV-vis absorptance and steady-state photoluminescence (PL) measurements of the neat perovskite thin films are shown in Figure S1 (Supporting Information (SI)). The absorptance spectrum of MAPI covers a spectral range up to 800 nm, whereas for the multi-cation lead mixed-halide, labeled as WBG-PVK, the absorption spectrum extends to 750 nm. The steady-

state PL spectrum exhibits a characteristic peak around 763 nm for MAPI, in contrast, the PL peak position is located at 739 nm for the WBG based PVK. This difference is in line with the expected difference in the perovskite's bandgap estimated to be ~1.59 eV and ~1.67 eV from the onset of the absorptance spectra (Figure S1), respectively. A difference in the energy of the valence band maximum (VBM) of ~0.1 eV was determined by ultraviolet photoelectron spectroscopy (UPS), the spectra are shown in Figure S2.

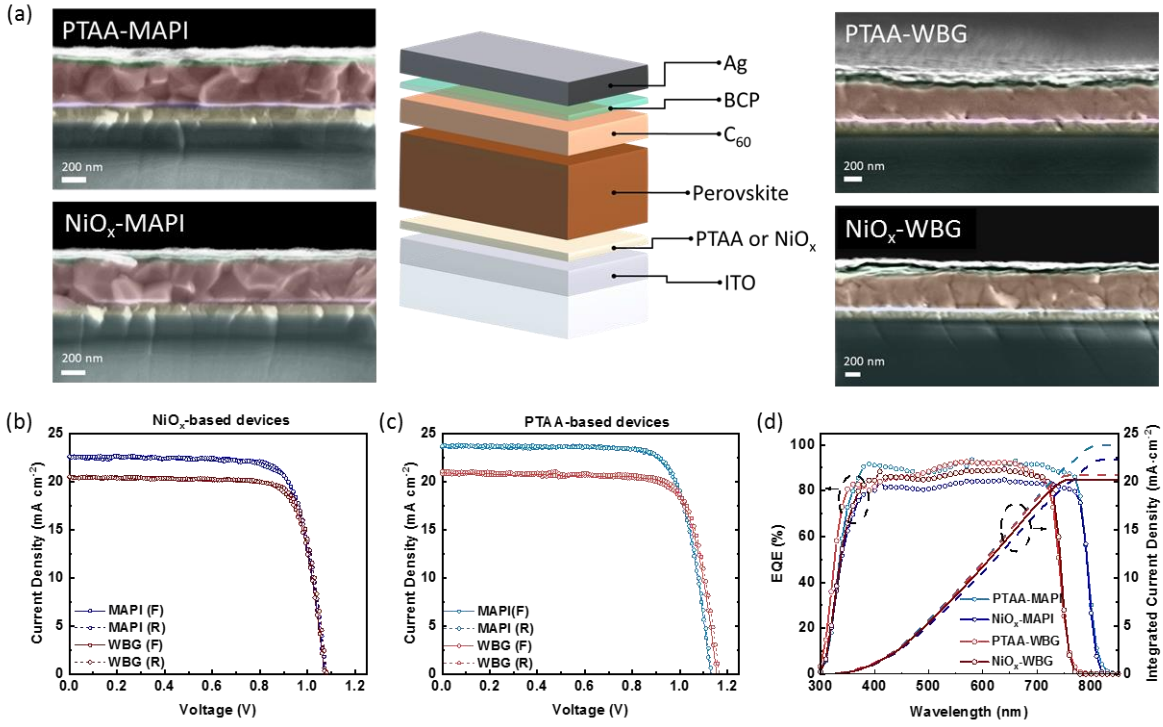

Figure 1: The cross-sectional SEM of the MAPI and WBG based devices, and the schematic of the device architecture. b) The *J–V* characteristics of the NiO_x-based devices and in c) the PTAA-based devices. d) The EQE spectra (open circles) of the corresponding devices alongside the integrated current density (dashed line).

To investigate the device performance of the NiO_x and PTAA-based solar cells, both narrow (1.59 eV) and wide bandgap (1.67 eV) PSCs were fabricated as described in the experimental section. The schematic of the *p-i-n* device stack (ITO/NiO_x or PTAA/PVK/C_{60}/BCP/Ag) used in this study

and cross-sectional scanning electron microscopy (SEM) images of the devices are shown in Figure 1a. MAPI films had a thickness of ~350 nm, whereas, WBG perovskite films had a thickness of ~450 nm. All perovskite films are formed with high-quality on both HTLs, namely, PTAA and NiO_x. The *J*−*V* characteristics and device parameters of the NiO_x- and PTAA-based PSCs are presented in Figures 1b and 1c, and Table 1, respectively. In particular, we found that the best performing device (PCE = 20.6%) is MAPI/PTAA, yielding the highest J_{SC} of 23.7 mA/cm^2 and V_{OC} of 1.13 V, while the WBG/PTAA resulted in a PCE = 19.0%. Here, the open-circuit voltage deficit (W_{OC}) of the MAPI and WBG based PTAA devices are 470 and 520 mV, respectively. In the case of NiO_x-based devices, we achieved a PCE of 18.6% for MAPI/NiO_x, whereas 17.4% is obtained for WBG/NiO_x. However, both devices yielded similar V_{OC} values, and the fill factor (FF) was almost identical across all four devices. Additionally, both the external quantum efficiency (EQE) and the integrated current density values of the devices matches (Figure 1d and Figure S4). The MAPI/PTAA device yields higher EQE in the spectral range from 350-450 nm. The absorptance spectrum of PTAA on ITO is shown in Figure S3, and comparing this to NiO_x reported earlier,[21] shows that the absorptance is higher for NiO_x. Additionally, the higher V_{OC} and J_{SC} values of PTAA-based devices (Figure S4) indicate that PTAA as HTL outperforms NiO_x. Below we outline the underlying reasons behind these findings and discuss the performance in terms of the photophysical processes tracked by transient optical measurements.

Table 1. *J*–*V* characteristic of champion PSCs with PTAA- and NiO_x-based HTLs.*

System	J_{SC} (mA cm^{-2})	V_{OC} (V)	FF (%)	PCE (%)	Scan direction
MAPI/NiO_x	22.6	1.08	76.1	18.6	Reverse
	22.5	1.07	77.0	18.6	Forward
WBG/NiO_x	20.5	1.08	78.5	17.4	Reverse
	20.5	1.07	77.5	17.0	Forward
MAPI/PTAA	23.7	1.13	76.7	20.6	Reverse
	23.6	1.13	77.0	20.5	Forward
WBG/PTAA	21.0	1.16	77.3	19.0	Reverse
	20.8	1.15	77.2	18.6	Forward

* All devices were tested at a 50 mV s^{-1} scan rate without any preconditioning.

To investigate the processes taking place at the PVK/HTL interface, transient optical measurements were performed on the PVK absorber layers adjacent to the HTLs upon optical excitation at 532 nm incident on the HTL side. Here, we use data from TR-PL and TA to get insight into interfacial charge recombination and charge extraction. The experimentally acquired TR-PL spectra of the different stacks MAPI/NiO_x, MAPI/PTAA, WBG/NiO_x, and WBG/PTAA at selected time delays are presented in Figure 2. For reference, the TR-PL spectra of neat PVK samples are presented in Figures S5 and S6 with the PL peak position of MAPI at 770 nm and of WBG at 739 nm.

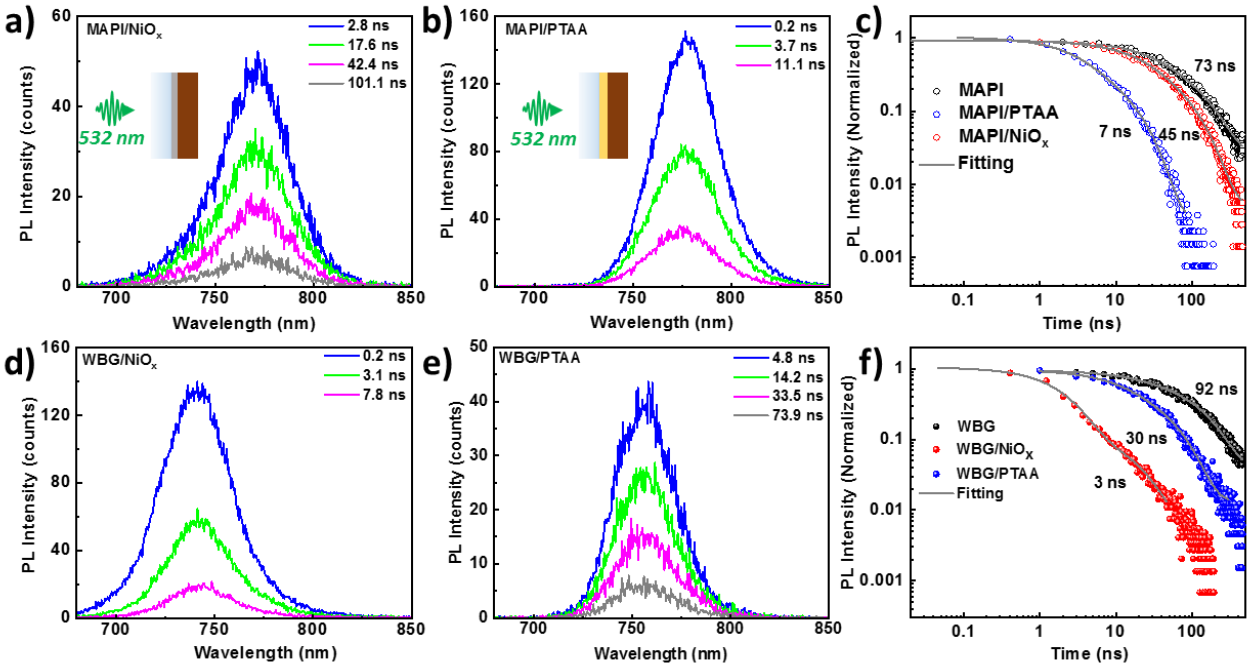

Figure 2: TR-PL spectra of representative perovskite stacks. a) The spectra of MAPI/NiO_x stack at different time delays upon photoexcitation at 532 nm using 300 nJ cm^{-2} fluence yielding initial carrier densities of $n_{0,MAPI}$ = 8.9 × 10^{16} cm^{-3} and $n_{0,WBG}$ = 6.9 × 10^{16} cm^{-3}. b) Spectra of MAPI/PTAA stack at selected time delays. c) Transients tracked at the PL peak of neat MAPI, MAPI/NiO_x stack with the fitting (solid grey lines) to a sum of two exponentials. d) time-integrated spectra of WBG/NiO_x stack. e) time-integrated spectra of WBG/PTAA. f) the associated transients of neat WBG based PVK, WBG/NiO_x, and WBG/PTAA stacks with the fits (solid grey lines).

The PL spectra of the different stacks are largely feature-less and transient spectral shifts are not observed. The PL of the WBG/PTAA sample peaks at ~756 nm with a shoulder around 739 nm at early delay times. We assign this to halide segregation as discussed in literature.[22] Further evaluation of the PL lifetime is done by tracking the PL decay at the respective PL peak positions. To this end, the neat WBG-PVK exhibits the longest PL lifetime of 92 ns compared to neat MAPI with 73 ns, when fitting to a two-exponential decay function (Table S1 and Table 2) and determining the average-weighted lifetimes according to: $(A_1t_1 \cdot A_2t_2)/(A_1+A_2)$, where A is the signal amplitude and t is the decay time, respectively. The overall shorter PL lifetime of MAPI is attributed to a higher density of traps, which is characteristic for this PVK.[23] Turning to the PVK/HTL stacks, the MAPI/NiO_x sample exhibits a faster PL decay of 45 ns, indicative of hole extraction from MAPI to NiO_x at early time scales; however, we assume that the PL decay also reflects in part interfacial charge recombination. Noteworthy, the PL of the MAPI/PTAA stack decays rapidly in 7 ns. Furthermore, the PL decay of the WBG/PTAA stack is shorter (30 ns) than that of the MAPI/PTAA stack. With this, the higher performance of the MAPI/PTAA-based device can be rationalized by efficient hole extraction, which yields the highest J_{SC} of all devices. In contrast, the WBG/NiO_x stack displays a substantially shortened PL lifetime of 3 ns. The initial fast PL decay component of the WBG/NiO_x transient is assigned to fast hole transfer, whereas the longer component is attributed to interfacial recombination. To evaluate this further, we performed TA experiments, as they can provide additional insight into charge transfer and non-radiative recombination processes and their dynamics.

Table 2: Parametrized averaged weighted lifetimes ($\tau_{wt,avg}$) of the representative systems of the TR-PL kinetics extracted as weighted averaged lifetimes.

Systems	$\tau_{avg,wt}$ **(ns)**
WBG	92
WBG/PTAA	30
WBG/NiO_x	3
MAPI	73
MAPI/PTAA	7

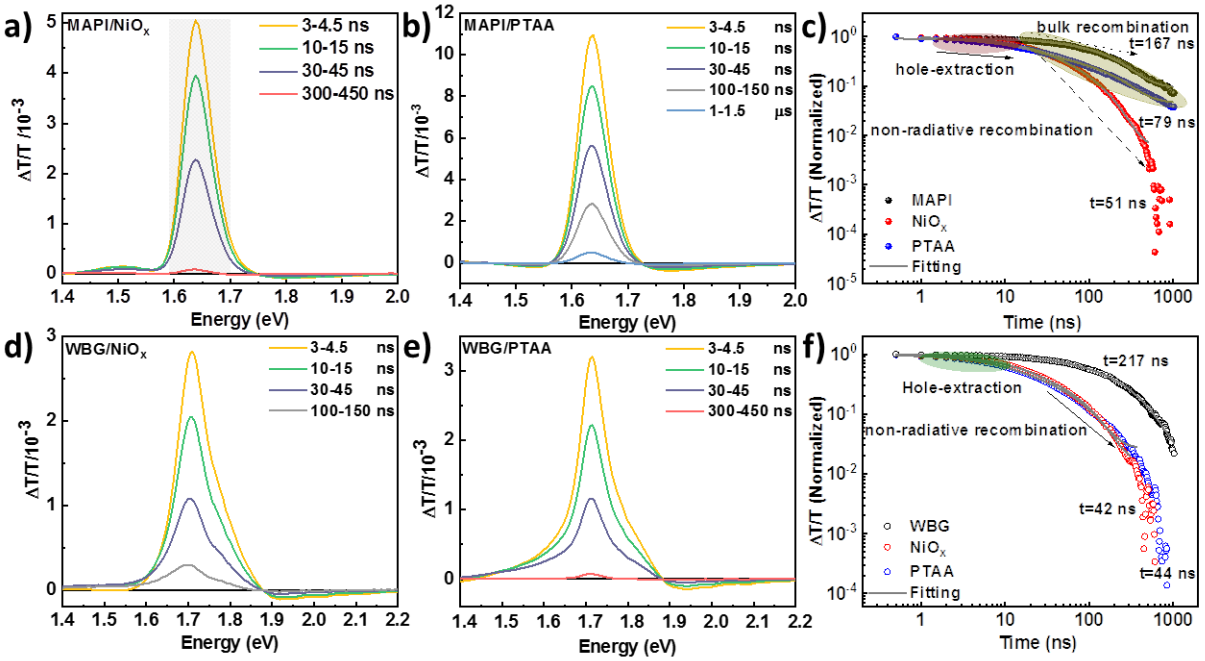

Figure 3: TA spectroscopy measurements upon optical excitation at 532 nm and 600 nJ cm^{-2} fluence yielding initial carrier densities ($n_{0,MAPI}$ = 1.8 × 10^{17} cm^{-3} and $n_{0,WBG}$ = 1.7 × 10^{17} cm^{-3}). The time-integrated spectra at different time delays of a) MAPI/NiO_x, the highlighted area is the GSB of MAPI, b) MAPI/PTAA, and c) kinetics of neat MAPI, MAPI/NiO_x, and MAPI/PTAA stacks extracted at the GSB. Time integrated TA spectra of d) WBG/NiO_x, e) WBG/PTAA, and f) kinetics of neat WBG based PVK, WBG/NiO_x, and WBG/PTAA stacks extracted at the GSB.

More precisely, we performed nanosecond-microsecond (ns-µs) TA spectroscopy on neat PVK thin films and the associated PVK/HTL stacks, the results are shown in Figure 3. The time-integrated probe spectra of neat MAPI and WBG PVK films at selected delay times are shown in Figures S7 and S8. The corresponding spectra of the stacks MAPI/NiO_x, MAPI/PTAA, WBG/NiO_x, and WBG/PTAA are presented in Figures 3a-3b and Figures 3d-3e. The TA spectra exhibit the characteristic GSB in the range of 1.58-1.73 eV (MAPI) and 1.54-1.85 eV (WBG), and a weak photo-induced absorption spanning from 1.73-2.00 eV (MAPI) and 1.86-2.20 eV (WBG).

Additionally, the associated kinetics extracted at the peak of the GSB at 1.65 eV and 1.70 eV of MAPI and WBG PVKs, respectively, are displayed in Figures 3c and 3f. The spectra of both PVKs are featureless, tracking the respective GSB decays, the WBG based PVK is found to exhibit slower dynamics than its counterpart (Table 3 and Table S2), which is consistent with the decay of the PL. The neat MAPI samples exhibits a single exponential and slow PL decay, which we assign to trap-assisted recombination of charges in the bulk. The GSB of MAPI/PTAA exhibits a slower decay than that of neat MAPI. Noteworthy, the decay is fast within the first 40 ns; however, beyond 40 ns it follows similar dynamics as observed in the neat MAPI. Hence, we assign this slower decay to electron-hole recombination in the bulk of MAPI and the faster decay is attributed to the extraction of holes to the PTAA transport layer. This is also consistent with the fast PL decay dynamics shown above (Figure 2c), which is attributed to hole extraction. With this, the higher J_{SC} for the MAPI/PTAA based device is due to less non-radiative recombination. In the case of MAPI/NiO_x, the GSB decay is substantially faster and displays different dynamics compared to the PTAA based stack. Initially, within the first 40 ns the decay is similar to the one in the PTAA based stack, which we ascribe to charge extraction. Subsequently, the decay is significantly faster than observed in both the pristine MAPI and MAPI/PTAA based samples on the same timescale, which we assign to interfacial non-radiative recombination. We note, that the lifetimes of MAPI/NiO_x extracted from TRPL (45 ns) and TA (51 ns) are comparable. The transients of both WBG/NiO_x and WBG/PTAA samples display similar dynamics as MAPI/NiO_x up to 200 ns, subsequently, the signal of the WBG/NiO_x stack decays faster then neat WBG. This implies that in WBG/NiO_x samples the hole extraction occurs at earlier times, whereas interfacial non-radiative recombination is dominant at longer times. In fact, this is in line with the observed lower J_{SC} in WBG/PTAA, yet the origin of such a small change of only 0.5 mA cm^{-2} in J_{SC} is difficult to unravel by transient measurements. We conclude that the MAPI/PTAA sample exhibits less interfacial non-radiative recombination leading to both higher J_{SC} and V_{OC}. In particular, the difference in V_{OC} is small, while a substantial difference in J_{SC} is observed when comparing MAPI and WBG based PVK devices. The difference to the WBG/NiO_x system is striking, it yields lower J_{SC} and V_{OC}. As discussed above, based on the absorptance measurements of the HTL, we exclude any impact from absorption in NiO_x and PTAA on J_{SC}. Hence, in the case of WBG/NiO_x and PTAA samples the TA dynamics and the TR-PL dynamics are comparable. For the MAPI/PTAA system our interpretation is distinct, as hole extraction is dominant at shorter time scales, which is confirmed

by both TA and TR-PL measurements. Additionally, the TA measurements reveal bulk recombination at longer time scales. For the case of sputtered NiO_x, our findings concerning the non-radiative recombination are in line with earlier reports in literature showing that interface passivation improves device performance in NiO_x-based devices.[24,25]

Table 3: Parametrized time constants t_1 and t_2 extracted from double exponential fits to the respective decays of the GSB and the extracted weighted-averaged $\tau_{TA,wt}$ lifetimes. Note the GSB decay of neat MAPI is fitted with a single exponential function.

Systems	**t_1 (ns)**	**t_2 (ns)**	**$\tau_{TA,wt}$ (ns)**
WBG	51	264	217
WBG/PTAA	12	80	44
WBG/NiO_x	15	77	42
MAPI	167	N/A	167
MAPI/PTAA	16	160	79
MAPI/NiO_x	20	84	51

The interfacial recombination depends not only on the defect density at the interface, but also on the conduction band offset (CBO) and valence band offset (VBO) between the electron transport layer (ETL)/PVK and HTL/PVK interfaces (i.e., PTAA's highest occupied molecular orbital (HOMO) and lowest unoccupied molecular orbital (LUMO)), which are both supported by simulations and experimentally verified. [26, 27] In particular, it was demonstrated that the VB of the HTL is lower than that of the perovskite absorber; an energy cliff is formed at the interface leading to the accumulation of holes. This non-favorable alignment of energy levels causes severe recombination and in turn reduces the V_{OC}.[28] Consequently, energy level alignment between HTL's and PVK's VBs reduces recombination and improves device performance. In order to evaluate the origin of the differences in V_{OC}, device drift-diffusion simulation was performed to provide further insight into the energetic landscape between the respective HTLs and PVKs. In particular, we have compared the simulated misalignment of the VB, which leads to an energy offset (ΔE) at the interface of HTL/PVK interface, with the experimentally achieved *Voc* losses. Furthermore, the

numerical model and analysis are detailed in the SI, andour calculations were performed under one sun illumination condition. In addition, the optical bandgaps (E_g), the thickness of the layers, the ionization potential (IP), and electron affinity (EA) inferred from IP + E_g or direct measurement related to both the active and additional layers used in the simulation are obtained from UPS and IPES measurements (Figure S2), results listed in Table S1, respectively. Specifically, the energy band diagrams of both PTAA- and NiO_x-based PSCs were computed and compared. We correlated the energy band alignment to determine band offsets at the respective PVK/HTL interfaces resulting in V_{OC} changes. Subsequently, the V_{OC} of the devices was determined and assessed by estimating the quasi-fermi level splitting (QFLS) from the band structure under one sun condition.[5,6] The V_{OC} and QFLS are considered equivalent under one-sun condition.[29] The quasi-Fermi levels for electrons and holes, E_{fn} and $E_{fp,}$ are the quantities representing the density of free photo-generated electrons (holes) in the conduction (valence) band within the limit of quasi-equilibrium as displayed in Figure 4, and the effective difference between E_{fn} and E_{fp} is QFLS.[26] In particular, quantifying QFLS has been an effective approach to investigate recombination losses in the PSCs.[30,31] Moreover, E_c and E_v are the energies related to the CB and VB edges, respectively, as shown in Figure 4. However, for the case of PTAA, the equivalent quantities are defined with respect to the HOMO and LUMO. In addition to the band-offset analysis, we have also considered interfacial electronic defects by adding a surface recombination velocity (SRV) to quantify the effect of surface passivation at PVK/NiO_x and PVK/PTAA interfaces. SRV is the surface equivalent of the minority carrier lifetime in a bulk semiconductor.[29] It can be used to provide insight into interfacial traps within the device stack. As pointed out in several earlier works, high SRV (~10^5 cm/s) and low minority carrier lifetime decrease the carrier density and carrier collected by the junction.[32,33]

Figure 4 presents the energy band diagrams associated with both PVK absorbers (MAPI and WBG) of PTAA and NiO_x based PSCs. In addition, the simulated E_{fn} and E_{fp} at V_{OC} are indicated by dotted lines (blue) with E_c and E_v of PTAA- and NiO_x-based PSCs in Figure 4. In the case of PTAA, we observe an energetically well-aligned HOMO (minimal energy offset) of the HTL layer with the MAPI and WBG devices as indicated by the solid lines (red) in Figure 4a and 4c, respectively. Subject to an ideal alignment, the photo-generated holes do not encounter any barrier and are collected efficiently at the front electrode. In addition, the PVK/PTAA sample exhibits less interfacial defects or traps, which leads to a $SRV_{PVK/PTAA}$ in the order of 10^2 cm/s.[32] Therefore,

PTAA acts as an ideal energetically well-aligned HTL for both MAPI and WBG based devices. Furthermore, we obtained a V_{OC} of 1.13 V and 1.15 V as depicted in Figures 4a and 4c for PTAA-based MAPI and WBG devices, respectively. On the other hand, we observe an energetically misaligned HTL layer in the case of NiO_x adjacent to MAPI and WBG-PVK in PSCs, as shown in Figures 4b and 4d.

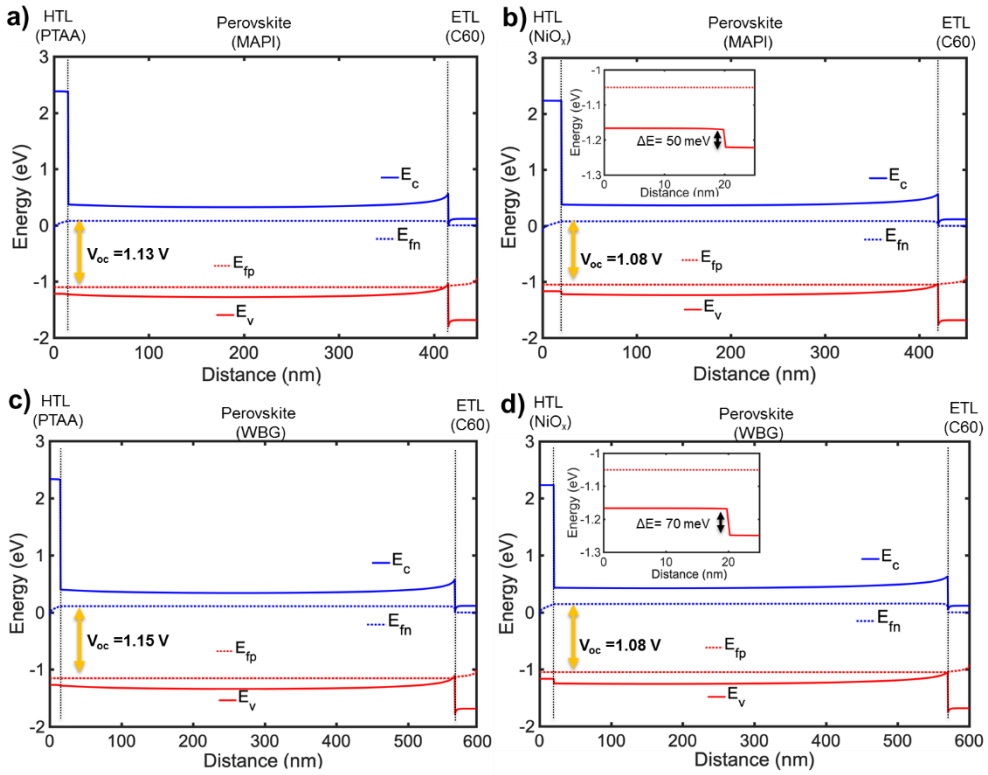

Figure 4: Simulated band diagram of the *p-i-n* structure of MAPI solar cells accounting with a) PTAA, and b) NiO_x, HTL interface at open circuit condition. Simulated band diagram of the *p-i-n* structure of WBG solar cells, accounting with c) PTAA, and d) NiO_x, HTL interface at open circuit condition. The respective insets in b) and d) display the energy offset between the respective valence bands of the PVKs and the HTLs.

This misalignment of the VB leads to an energy offset (ΔE) causing an increase of the hole population at the HTL (NiO_x) interface,[6] resulting in higher recombination rate due to a higher $SRV_{PVK/NiOx}$ in the order of 10^5 cm/s.[7] The simulation indicates notable energy barriers of 50 meV

and 70 meV at the MAPI/NiO_x and WBG/NiO_x interfaces, respectively, as shown in the insets of Figures 4b and 4d. This directly correlates with the loss in V_{OC} observed in our experimentally measured device characteristics shown in Table 1**.** Furthermore, our simulation yields a V_{OC} of 1.08 V for both NiO_x-based MAPI and WBG devices as shown in Figures 4c and 4d, which matches the experimentally determined value. Hence, expectedly a finite ΔE results in an equal loss in the device V_{OC}. Besides, we conclude that the band-offset at the MAPI/HTL and WBG/HTL interface is a crucial factor determining carrier recombination at the interface, which governs the V_{OC}.

The simulation confirms the findings from the time-resolved measurements, which indicated effectual extraction and reduced non-radiative interfacial recombination associated with the MAPI/PTAA interface, leading to both improved V_{OC} and J_{SC}. In addition, the unfavorable band alignment in the case of the WBG/NiO_x interface leads to considerable non-radiative recombination, which is confirmed by TA measurements, caused by the offset ΔE of 70 meV. Hence, the loss in V_{OC} can be rationalized by the energy offset. Thus, we find an excellent agreement between the simulation and our spectroscopic results. Briefly, the MAPI/NiO_x stack exhibits moderate PL quenching and substantial non-radiative recombination as seen by TA, caused by the unfavorable band alignment with a ΔE of 50 meV, causing the drop in V_{OC}. Finally, the WBG/PTAA stack exhibits mainly non-radiative recombination, which limits the J_{SC}, as confirmed by the TA measurements. However, due to the more favorable energy level alignment, the V_{OC} is not affected, as supported by the simulation. Finally, our simulation is validated by reconstructing the experimentally-measured *J-V* characteristics of MAPI/PTAA- and MAPI/NiO_x-based devices using the simulated parameters. The results are shown in Figure S9, they demonstrate that both the experimentally and simulated *J-V* curves are in good agreement.

The interfacial recombination at the MAPI/NiO_x and MAPI/PTAA interfaces is further studied using impedance spectroscopy. Figures 5a and 5b show the impedance spectra of both devices taken under open circuit condition at 100 mW/cm^2 illumination. As shown in the inset of Figure 5c, equivalent circuits with two arcs are used to parameterize the data. The arc in the high-frequency region (>1kHz) represents carrier recombination (R_2) and the dielectric properties (C_g) of the bulk perovskite layer, whereas the low-frequency region arc (~1Hz) is caused by the recombination resistance (R_3) and charge accumulation capacitance (C_s) at the perovskite layer interfaces. Since recombination and photo-generation currents cancel each other at open circuit

conditions, recombination resistance at this point given by the R_2+R_3 represents the trap-related recombination. Therefore, higher recombination resistance of MAPI/PTAA results from the lower interfacial trap density.[34] In contrast, the MAPI/NiO_x interface yields a lower resistance, implying higher interfacial trap density (Figure 5).

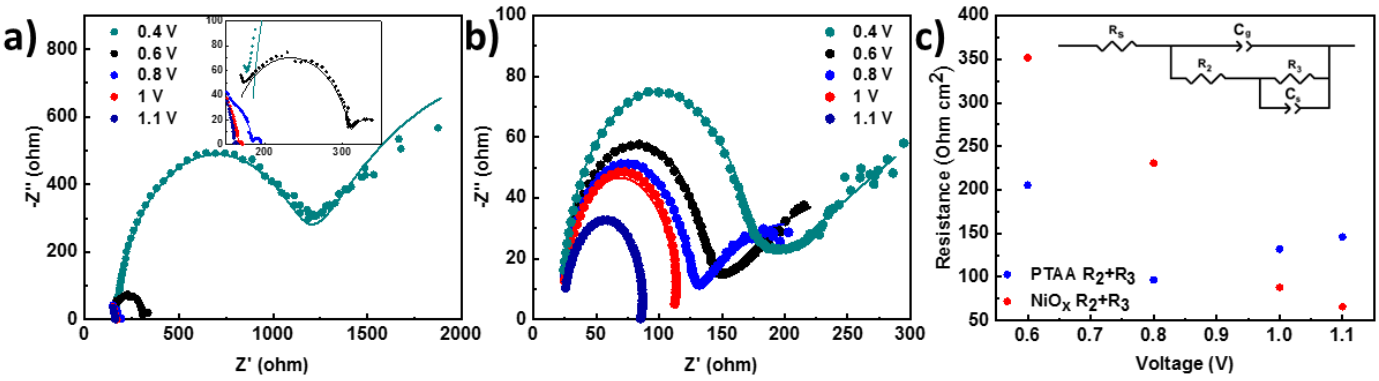

Figure 5: Nyquist plots of a) MAPI/PTAA with voltage range of 0.4-1.1 V, and the inset displays the voltage range 0.6-1.0 V. In b) MAPI/NiO_x devices under 1-sun light illumination at different bias voltages, c) low-frequency resistance of NiO_x and PTAA based HTL devices with respect to the applied bias voltages, with the inset showing the equivalent circuit, here R_S is the serial resistance.

In conclusion, we studied two HTLs, namely, PTAA and NiO_x, adjacent to either MAPI or a WBG-PVK in PSCs. MAPI/PTAA based devices yielded the highest performance due to a high J_{SC} (23.7 mA cm^{-2}) and V_{OC} (1.13 V). By combining TR-PL and TA spectroscopy data, we confirmed that the shortened PL lifetime observed in MAPI/PTAA stacks is due to effectual hole extraction. Additionally, TA measurements also revealed reduced non-radiative interfacial recombination. In general, our results show that PTAA as HTL outperforms NiO_x due to less non-radiative recombination, indicative of lower interfacial trap state density. Furthermore, drift-diffusion simulations supported the results of transient measurements. In particular for NiO_x-based devices, the energy band offset between the valence band of the respective perovskites and NiO_x is 50 meV (WBG/NiO_x) and 70 meV (MAPI/NiO_x), which causes substantial interfacial non-radiative recombination in the MAPI/NiO_x stack. Finally, impedance spectroscopy measurements further

confirmed higher recombination resistance at the MAPI/NiO_x interface compared to the MAPI/PTAA interface.

Experimental section

Device fabrication and characterization of single-junction perovskite solar cells: The inverted (*p*−*i*−*n*) device stack consists of ITO-hole transporting layer (HTL)-Perovskite-C_{60}-BCP-Ag. The devices were prepared using the following procedure. ITO coated substrates were cleaned by sonication successively in detergent, deionized water, acetone, and isopropanol for 15 min, respectively. They were then dried with N_2 flow and transferred to an N_2-filled glovebox. The PTAA (2 mg/ml in CB) HTL with a thickness of ~15 nm was spin-coated on top of the ITO at 6000 rpm for 20 s and subsequently annealed at 100 °C for 10 min. The NiOx HTL layer was deposited by radio frequency (RF) magnetron sputtering from a stoichiometric NiO target (99.95% purity) at room temperature using Angstrom Engineering EvoVac system.[20] To coat the $MAPbI_3$ perovskite layer, 1.10 M equimolar MAI and PbI_2 were dissolved in co-solvent of dimethylformamide/dimethyl sulfoxide (DMF/DMSO; 4/1:v/v). For the wide-bandgap perovskite, the perovskite precursor solution was prepared by dissolving CsI, FAI, MABr, PbI_2, and $PbBr_2$ in co-solvent of DMF/DMSO (4/1:v/v) to obtain 1.25 M of $Cs_{0.15}MA_{0.15}FA_{0.70}Pb(I_{0.80}Br_{0.20})_3$. The perovskite solutions were then coated onto the PTAA or NiO_x layers using a consecutive two-step spin-coating process consisting of 2000 rpm for 10 s and 5000 rpm for 30 s. 300 µl of EtAc was dropped at the 10th s of the second step. The films $MAPbI_3$ films were annealed at 100 °C for 15 minutes, whereas, the $Cs_{0.15}MA_{0.15}FA_{0.70}Pb(I_{0.80}Br_{0.20})_3$ films were annealed at 100 °C for 30 minutes. The devices were completed by thermal deposition of 30 nm-thick C_{60}, 8 nm-thick BCP, and 100 nm-thick Ag top contact at a vacuum of $<3\times10^{-6}$ Torr. All devices were tested using a Keithley 2400 at room temperature under AM 1.5G illuminations (1000 W/m^2) with an Abet Technologies Sun 3000 solar simulator, which was calibrated using a standard silicon cell (RERA). Current density-voltage (*J*−*V*) curves were obtained both in reverse (1.2 V → -0.1 V) and forward scan (-0.1 V → 1.2 V) with a step size of 10 mV. All the measurements were performed under an N_2 environment inside the glovebox.

External quantum efficiency (EQE): The EQE of solar cells was measured with a Newport EQE system (Model: Oriel IQE-200) by focusing the chopped monochromatic light beam onto the active area of the solar cells without external white-light bias.

Scanning electron microscopy (SEM): SEM images were obtained with a ZEISS Auriga Crossbeam system with an accelerating voltage of 5 kV.

UV-vis absorption spectroscopy: The transmittance (T) and reflectance (R) of the perovskite samples were obtained between 350 and 900 nm using a Perkin Elmer Lambda 950 UV-vis-NIR (near-infrared) spectrophotometer equipped with an integrated sphere. Particularly, the absorptance (A) of the films was calculated by following relation A=1-(T+R), where T and R are the measured transmittance and reflectance, respectively

Photoluminescence (PL): The PL spectra of the samples were collected using Horiba FluoroMax-4 spectrofluorometer following an optical excitation at 550 nm.

Transient absorption (TA): (TA) spectroscopy was carried out using a home-built pump-probe setup. Two distinct configurations of the setup were applied for either short delay, namely 100 fs to 8 ns experiments, or long delay, namely 1 ns to 100 μs delays, as described below.

For the 1 ns to 100 μs delay (long delay) TA measurements in the range covering 500-1500 nm, we used the fundamental 800 nm output of titanium:sapphire amplifier (Coherent LEGEND DUO, 4.5 mJ, 3 kHz, 100 fs) focused onto a sapphire crystal, thereby generating a white-light supercontinuum from 500 to 1500 nm. However, the excitation light (pump pulse) was provided by an actively Q-switched Nd:YVO_4 laser (INNOLAS picolo AOT) frequency-doubled to provide pulses at 532 nm. The laser was triggered by an electronic delay generator (Stanford Research Systems DG535), itself triggered by the TTL sync from the Legend DUO, allowing control of the delay between pump and probe with a jitter of roughly 100 ps.

Pump and probe beams were focused on the sample, which was kept under a dynamic vacuum of $<10^{-5}$ mbar. The transmitted fraction of the white light was guided to a custom-made prism spectrograph (Entwicklungsbüro Stresing) where a prism dispersed it onto a 512 pixel NMOS linear image sensor (HAMAMATSU S8381-512). The probe pulse repetition rate was 3 kHz, directly generated at 1.5 kHz frequency (1 ns to 100 μs delays), while the detector array was read out at 3 kHz. Adjacent diode readings corresponding to the transmission of the sample after excitation and in the absence of an excitation pulse were used to calculate $\Delta T/T$. Measurements were averaged over several thousand shots to obtain a good signal-to-noise ratio. The chirp induced

by the transmissive optics was corrected with a home-built Matlab code by revaluating for each wavelength the delay at which pump and probe are simultaneously arriving on the sample as the time of the signal amplitude.

Time-resolved photoluminescence spectroscopy (TR-PL): For TR-PL experiments samples were excited with the Coherent Helios 532 nm nanosecond laser with a pulse width of 0.85 nanosecond (ns) and a repetition rate of 1 kHz. Typical fluences were in the range of 300 nJ/cm^2. The PL of the samples was collected by an optical telescope (consisting of two plano-convex lenses), and it was further focused on the slit of a spectrograph (PI Spectra Pro SP2300), and eventually detected with a Streak Camera (Hamamatsu C10910) system with a temporal resolution of 1.4 picosecond (ps). The data was acquired in photon counting mode using the Streak Camera software (HPDTA) and was exported to Origin Pro 2020 for further analysis. All samples were kept in a nitrogen-filled chamber and measured at room temperature.

Ultraviolet photoelectron spectroscopy (UPS) and Inverse Photoemission spectroscopy (IPES): Photoemission spectroscopy was conducted in a single multi-probe UHV (ultrahigh vacuum) chamber (ScientaOmicron) operating at 10^{-10} mbar. This was equipped with an attenuated (reduced copper slit aperture) He(1) source 21.22 eV with a Spehera II EAC 125 hemispherical electron analyzer. The XPS (x-ray photoelectron spectroscopy) was performed with a monochromated XM1000 source with Al Kα. IPES (inverse photoemission spectroscopy) was performed using a home-built setup consisting of a light isolated sphere chamber equipped with a STAIB BaO cathode electron source operating at 20-30 eV beam energy with a dispersion of energy 0.25-0.5 eV. A +20 V bias was applied to the sample to result in effective kinetic energies of 0-6 eV. All light sources were eliminated and the emitted IPES radiation was detected using a band pass filters (Semrock) of 4.88 or 4.43 eV energy and a photon multiplier tube (PMT) at 940 V.

Samples for both UPS and IPES were mounted on Omicron style holding plates placed in good electrical contact to the analyzer. UPS scans were performed prior to XPS analysis at 10 or 5 eV constant pass energy. Subsequent scans were monitored to determine any radiation-induced charging during the measurements. Calibration of the analyzer work function was made by a sputter cleaned Au film measured prior to measurement of the presented spectra. IPES

measurements were conducted in the bremsstrahlung isochromatic mode directly after UPS without exposing to air. The +20V bias was applied to the sample and a linear beam energy scan was made while simultaneously measuring the sample drain current and photon intensity. The turn-on energy was found by differentiation and then fitting a Gaussian function, to calibrate the spectra from the vacuum level ($E_0 + hv_{bp} = E_{vac}$) and therefore extract electron affinities.

The UPS spectra were analyzed in the following way: Firstly, the work functions were determined by a linear extrapolation of the secondary electron cut-off taking into account the incident He(1) energy 21.22 eV. The He(1) satellites at 23.07 (1.87%) and 23.74 (0.035%) contributions erewere deducted from the spectra by comparison to measurement on the Ef step of clean Au. Secondly, the valence band or HOMO (highest occupied molecular orbital) were identified by fitting Gaussian functions at the edges and using 2σ for the NiO_x and PTAA and 2.9σ for the Pb halide perovskite films. For the latter, this follows the previous methodology demonstrated that both theoretically and experimentally, where the Pb halide film is best viewed in a semi-log plot to account for the low intensity of the valence band photoemission at the spectra edge. The IPES spectra for PTAA and NiO_x are tentatively analyzed placing the CBM (conduction band maximum)/LUMO (lowest unoccupied molecular orbital) energy level at the leading edge of spectra, consistent with a previous study which shas identified intensity beyond the edges in PTAA. The perovskite CBM was determined from the optical band gap (VBM + E_g(optical)) where the exciton binding energy is small enough to be negligible 15 meV. The energy level diagram was then constructed viewed from the vacuum level (local) being aligned for all samples.

Impedance spectroscopy: The measurements are performed in the N_2 atmosphere with Autolab PGSTAT302N potentiostat in the range of 1MHz to 1Hz with 10 mV AC perturbation. A waiting period of 2 minutes in dark is applied between the measurements. The data is collected with NOVA 2.5 software and analyzed with Z-view software.

AUTHOR INFORMATION

Corresponding Authors

frederic.laquai@kaust.edu.sa

jafar.khan@kaust.edu.sa

Webpage:

Ultrafast Dynamics Group: https://ufd.kaust.edu.sa

Orcid:

Jafar I. Khan: 0000-0001-6003-5641

Frédéric Laquai: 0000-0002-5887-6158

Notes

The authors declare no competing financial interest.

ACKNOWLEDGMENT

This publication is based upon work supported by the King Abdullah University of Science and Technology (KAUST) Office of Sponsored Research (OSR) under Award No: OSR-2018-CARF/CCF-3079.

Supporting Information

Supporting Information is available from the Online Library or from the authors.

Steady state spectroscopy, energetics, absorptance, device characteristics, time resolved photoluminescence, TA results, device simulation.

References

1. NREL Best Research-Cell Efficiency Chart. Https://Www.Nrel.Gov/Pv/Cell-Efficiency.Html. (Accessed October 2021)
2. Zuo, C.; Bolink, H. J.; Han, H.; Huang, J.; Cahen, D.; Ding, L., Advances In Perovskite Solar Cells. *Adv. Sci.* **2016**, *3* (7), 1500324.
3. Calió, L.; Kazim, S.; Grätzel, M.; Ahmad, S., Hole-Transport Materials For Perovskite Solar Cells. *Angew. Chem. Int. Ed.* **2016**, *55* (47), 14522-14545.
4. Isikgor, F. H.; Subbiah, A. S.; Eswaran, M. K.; Howells, C. T.; Babayigit, A.; De Bastiani, M.; Yengel, E.; Liu, J.; Furlan, F.; Harrison, G. T.; Zhumagali, S.; Khan, J. I.; Laquai, F.; Anthopoulos, T. D.; Mcculloch, I.; Schwingenschlögl, U.; De Wolf, S., Scaling-Up Perovskite Solar Cells On Hydrophobic Surfaces. *Nano Energy* **2021**, *81*, 105633.
5. Zhumagali, S.; Isikgor, F. H.; Maity, P.; Yin, J.; Ugur, E.; De Bastiani, M.; Subbiah, A. S.; Mirabelli, A. J.; Azmi, R.; Harrison, G. T.; Troughton, J.; Aydin, E.; Liu, J.; Allen, T.; Rehman, A. u.; Baran, D.; Mohammed, O. F.; De Wolf, S., Linked Nickel Oxide/Perovskite Interface Passivation For High-Performance Textured Monolithic Tandem Solar Cells. *Adv. Energy Mater.* **2021**, 2101662.
6. Stolterfoht, M.; Caprioglio, P.; Wolff, C. M.; Márquez, J. A.; Nordmann, J.; Zhang, S.; Rothhardt, D.; Hörmann, U.; Amir, Y.; Redinger, A.; Kegelmann, L.; Zu, F.; Albrecht, S.; Koch, N.; Kirchartz, T.; Saliba, M.; Unold, T.; Neher, D., The Impact Of Energy Alignment And Interfacial Recombination On The Internal And External Open-Circuit Voltage Of Perovskite Solar Cells. *Energy Environ. Sci.* **2019**, *12* (9), 2778-2788.
7. Boyd, C. C.; Shallcross, R. C.; Moot, T.; Kerner, R.; Bertoluzzi, L.; Onno, A.; Kavadiya, S.; Chosy, C.; Wolf, E. J.; Werner, J.; Raiford, J. A.; De Paula, C.; Palmstrom, A. F.; Yu, Z. J.; Berry, J. J.; Bent, S. F.; Holman, Z. C.; Luther, J. M.; Ratcliff, E. L.; Armstrong, N. R.; Mcgehee, M. D., Overcoming Redox Reactions At Perovskite-Nickel Oxide Interfaces To Boost Voltages In Perovskite Solar Cells. *Joule* **2020**, *4* (8), 1759-1775.
8. Zhang, S.; Shaw, P. E.; Zhang, G.; Jin, H.; Tai, M.; Lin, H.; Meredith, P.; Burn, P. L.; Neher, D.; Stolterfoht, M., Defect/Interface Recombination Limited Quasi-Fermi Level Splitting And Open-Circuit Voltage In Mono- And Triple-Cation Perovskite Solar Cells. *ACS Appl. Mater. Interfaces* **2020**, *12* (33), 37647-37656.
9. Krogmeier, B.; Staub, F.; Grabowski, D.; Rau, U.; Kirchartz, T., Quantitative Analysis Of The Transient Photoluminescence Of $CH_3NH_3PbI_3/PC_{61}BM$ Heterojunctions By Numerical Simulations. *Sustain. Energy Fuels* **2018**, *2* (5), 1027-1034.
10. Song, D.; Ji, J.; Li, Y.; Li, G.; Li, M.; Wang, T.; Wei, D.; Cui, P.; He, Y.; Mbengue, J. M., Degradation Of Organometallic Perovskite Solar Cells Induced By Trap States. *Appl. Phys. Lett.* **2016**, *108* (9), 093901.
11. Yin, X.; Song, Z.; Li, Z.; Tang, W., Toward Ideal Hole Transport Materials: A Review On Recent Progress In Dopant-Free Hole Transport Materials For Fabricating Efficient And Stable Perovskite Solar Cells. *Energy Environ. Sci.* **2020**, *13* (11), 4057-4086.
12. Haddad, J.; Krogmeier, B.; Klingebiel, B.; Krückemeier, L.; Melhem, S.; Liu, Z.; Hüpkes, J.; Mathur, S.; Kirchartz, T., Analyzing Interface Recombination In Lead-Halide Perovskite Solar Cells With Organic And Inorganic Hole-Transport Layers. *Adv. Mater. Interfaces* **2020**, *7* (16), 2000366.

13. Eom, K.; Kwon, U.; Kalanur, S. S.; Park, H. J.; Seo, H., Depth-Resolved Band Alignments Of Perovskite Solar Cells With Significant Interfacial Effects. *J. Mater. Chem. A* **2017**, *5* (6), 2563-2571.
14. Song, J.-X.; Yin, X.-X.; Li, Z.-F.; Li, Y.-W., Low-Temperature-Processed Metal Oxide Electron Transport Layers For Efficient Planar Perovskite Solar Cells. *Rare Metals,* **2021**, 40, 2730-2746.
15. Ugur, E.; Khan, J. I.; Aydin, E.; Wang, M.; Kirkus, M.; Neophytou, M.; Mcculloch, I.; De Wolf, S.; Laquai, F., Carrier Extraction From Perovskite To Polymeric Charge Transport Layers Probed By Ultrafast Transient Absorption Spectroscopy. *J. Phys. Chem. Lett.* **2019**, *10* (21), 6921-6928.
16. Kirchartz, T.; Márquez, J. A.; Stolterfoht, M.; Unold, T., Photoluminescence-Based Characterization Of Halide Perovskites For Photovoltaics. *Adv. Energy Mater.* **2020**, *10* (26), 1904134.
17. Krückemeier, L.; Krogmeier, B.; Liu, Z.; Rau, U.; Kirchartz, T., Understanding Transient Photoluminescence In Halide Perovskite Layer Stacks And Solar Cells. *Adv. Energy Mater.* **2021**, *11* (19), 2003489.
18. Tress, W., Perovskite Solar Cells On The Way To Their Radiative Efficiency Limit – Insights Into A Success Story Of High Open-Circuit Voltage And Low Recombination. *Adv. Energy Mater.* **2017**, *7* (14), 1602358.
19. Pisoni, S.; Stolterfoht, M.; Löckinger, J.; Moser, T.; Jiang, Y.; Caprioglio, P.; Neher, D.; Buecheler, S.; Tiwari, A. N., On The Origin Of Open-Circuit Voltage Losses In Flexible N-I-P Perovskite Solar Cells. *Sci. Technol. Adv. Mater.* **2019**, *20* (1), 786-795.
20. Isikgor, F. H.; Furlan, F.; Liu, J.; Ugur, E.; Eswaran, M. K.; Subbiah, A. S.; Yengel, E.; De Bastiani, M.; Harrison, G. T.; Zhumagali, S.; Howells, C. T.; Aydin, E.; Wang, M.; Gasparini, N.; Allen, T. G.; Rehman, A. U.; Van Kerschaver, E.; Baran, D.; Mcculloch, I.; Anthopoulos, T. D.; Schwingenschlögl, U.; Laquai, F.; De Wolf, S., Concurrent Cationic And Anionic Perovskite Defect Passivation Enables 27.4% Perovskite/Silicon Tandems With Suppression Of Halide Segregation. *Joule* **2021**, *5* (6), 1566-1586.
21. Aydin, E.; Troughton, J.; De Bastiani, M.; Ugur, E.; Sajjad, M.; Alzahrani, A.; Neophytou, M.; Schwingenschlögl, U.; Laquai, F.; Baran, D.; De Wolf, S., Room-Temperature-Sputtered Nanocrystalline Nickel Oxide As Hole Transport Layer For P–I–N Perovskite Solar Cells. *ACS Appl. Energy Mater.* **2018**, *1* (11), 6227-6233.
22. Knight, A. J.; Borchert, J.; Oliver, R. D. J.; Patel, J. B.; Radaelli, P. G.; Snaith, H. J.; Johnston, M. B.; Herz, L. M., Halide Segregation In Mixed-Halide Perovskites: Influence Of A-Site Cations. *ACS Energy Lett.* **2021**, *6* (2), 799-808.
23. Feldmann, S.; Macpherson, S.; Senanayak, S. P.; Abdi-Jalebi, M.; Rivett, J. P. H.; Nan, G.; Tainter, G. D.; Doherty, T. A. S.; Frohna, K.; Ringe, E.; Friend, R. H.; Sirringhaus, H.; Saliba, M.; Beljonne, D.; Stranks, S. D.; Deschler, F., Photodoping Through Local Charge Carrier Accumulation In Alloyed Hybrid Perovskites For Highly Efficient Luminescence. *Nat. Photonics* **2020**, *14* (2), 123-128.
24. Zheng, X.; Song, Z.; Chen, Z.; Bista, S. S.; Gui, P.; Shrestha, N.; Chen, C.; Li, C.; Yin, X.; Awni, R. A.; Lei, H.; Tao, C.; Ellingson, R. J.; Yan, Y.; Fang, G., Interface Modification Of Sputtered Niox As The Hole-Transporting Layer For Efficient Inverted Planar Perovskite Solar Cells. *J. Mater. Chem. C* **2020,** *8* (6), 1972-1980.
25. Pant, N.; Kulkarni, A.; Yanagida, M.; Shirai, Y.; Yashiro, S.; Sumiya, M.; Miyasaka, T.; Miyano, K., Passivation Of Bulk And Interface Defects In Sputtered-Niox-Based Planar

Perovskite Solar Cells: A Facile Interfacial Engineering Strategy With Alkali Metal Halide Salts. *ACS Appl. Energy Mater.* **2021,** *4* (5), 4530-4540.

26. Dong, J.; Shi, J.; Li, D.; Luo, Y.; Meng, Q., Controlling The Conduction Band Offset For Highly Efficient Zno Nanorods Based Perovskite Solar Cell. *Appl. Phys. Lett.* **2015**, *107* (7), 073507.

27. Ding, C.; Zhang, Y.; Liu, F.; Kitabatake, Y.; Hayase, S.; Toyoda, T.; Yoshino, K.; Minemoto, T.; Katayama, K.; Shen, Q., Effect Of The Conduction Band Offset On Interfacial Recombination Behavior Of The Planar Perovskite Solar Cells. *Nano Energy* **2018**, *53*, 17-26.

28. Minemoto, T.; Murata, M., Theoretical Analysis On Effect Of Band Offsets In Perovskite Solar Cells. *Sol. Energy Mater. Sol. Cells* **2015**, *133*, 8-14.

29. Caprioglio, P.; Stolterfoht, M.; Wolff, C. M.; Unold, T.; Rech, B.; Albrecht, S.; Neher, D., On The Relation Between The Open-Circuit Voltage And Quasi-Fermi Level Splitting In Efficient Perovskite Solar Cells. *Adv. Energy Mater.* **2019**, *9* (33), 1901631.

30. Stolterfoht, M.; Wolff, C. M.; Márquez, J. A.; Zhang, S.; Hages, C. J.; Rothhardt, D.; Albrecht, S.; Burn, P. L.; Meredith, P.; Unold, T.; Neher, D., Visualization And Suppression Of Interfacial Recombination For High-Efficiency Large-Area Pin Perovskite Solar Cells. *Nat. Energy* **2018**, *3* (10), 847-854.

31. Sarritzu, V.; Sestu, N.; Marongiu, D.; Chang, X.; Masi, S.; Rizzo, A.; Colella, S.; Quochi, F.; Saba, M.; Mura, A.; Bongiovanni, G., Optical Determination Of Shockley-Read-Hall And Interface Recombination Currents In Hybrid Perovskites. *Sci. Rep.* **2017**, *7* (1), 44629.

32. Wang, J.; Fu, W.; Jariwala, S.; Sinha, I.; Jen, A. K. Y.; Ginger, D. S., Reducing Surface Recombination Velocities At The Electrical Contacts Will Improve Perovskite Photovoltaics. *ACS Energy Lett.* **2019**, *4* (1), 222-227.

33. Bertoluzzi, L.; Boyd, C. C.; Rolston, N.; Xu, J.; Prasanna, R.; O'Regan, B. C.; Mcgehee, M. D., Mobile Ion Concentration Measurement And Open-Access Band Diagram Simulation Platform For Halide Perovskite Solar Cells. *Joule* **2020**, *4* (1), 109-127.

34. Yang, Y.; Hoang, M. T.; Yao, D.; Pham, N. D.; Tiong, V. T.; Wang, X.; Wang, H., Spiro-Ometad Or Cuscn As A Preferable Hole Transport Material For Carbon-Based Planar Perovskite Solar Cells. *J. Mater. Chem. A* **2020**, *8* (25), 12723-12734.